# Intravital calcium imaging of meningeal macrophages reveals niche-specific dynamics and aberrant responses to brain hyperexcitability

Simone Carneiro-Nascimento[1], Chao Wei[1], Anna Gutterman[1], Dan Levy[1*]

*Correspondence:

Dan Levy

dlevy1@bidmc.harvard.edu

[1]Department of Anesthesia, Critical Care and Pain Medicine, Beth Israel Deaconess Medical Center, Harvard Medical School, Boston, United States

# Abstract

The meninges, which envelop and protect the brain, host a dense network of resident macrophages with diverse roles in regulating homeostasis and neuroinflammation. Despite their importance, we have a limited understanding of their behavior in vivo. Many dynamic cellular functions of macrophages involve intracellular $Ca^{2+}$ signaling. However, to our knowledge, virtually nothing is known about the spatiotemporal $Ca^{2+}$ dynamics of meningeal macrophages. We developed a chronic intravital two-photon imaging approach and related computational analysis tools to interrogate meningeal macrophage $Ca^{2+}$ dynamics, at a subcellular resolution, in a novel $Pf4^{Cre}$:TIGRE2.$0^{GCaMP6s/wt}$ reporter mouse model. Using imaging in awake mice, we characterized the $Ca^{2+}$ activity of meningeal macrophages at steady state and in response to cortical spreading depolarization (CSD), an aberrant pro-inflammatory brain hyperexcitability event, implicated in migraine, traumatic brain injury, and stroke. In homeostatic meninges, macrophages in the dural perivascular niche exhibited several $Ca^{2+}$ dynamic features, including event duration and signal frequency spectrum, distinct from those of in the interstitial, non-perivascular niche. Simultaneous tracking of meningeal macrophage $Ca^{2+}$ dynamics and local vasomotion revealed a subset of dural perivascular macrophages whose activity was coupled to behaviorally-driven diameter fluctuations of their associated vessels. Most perivascular and non-perivascular meningeal macrophages displayed propagating intracellular $Ca^{2+}$ activity as well as synchronized intercellular $Ca^{2+}$ elevations, likely driven by extrinsic factors. In response to CSD, the majority of perivascular and non-perivascular meningeal macrophages showed a persistent decrease in $Ca^{2+}$ activity, while a smaller subset displayed $Ca^{2+}$ elevations.

Mechanistically, CGRP/RAMP1 signaling mediated the increase but not the decrease in CSD-mediated $Ca^{2+}$ signaling. Collectively, our results highlight a previously unknown diversity of meningeal macrophage $Ca^{2+}$ dynamics at steady state and in response to an aberrant brain hyperexcitability event linked to neuroinflammation.

**Keywords:** Meningeal macrophages, calcium imaging, dural vasomotion, cortical spreading depolarization, migraine

# Introduction

Resident macrophages are key myeloid immunocytes that play an important role in innate immune surveillance and defense across various peripheral tissues and organs [1-3]. The central nervous system also harbors a large subset of parenchymal macrophages, known as microglia, and several distinct subsets of macrophages localized to the brain's border tissues, including the choroid plexus, perivascular spaces, and the meningeal compartments that cover, protect, and support the brain [4-8]. Macrophages are the predominant immune cell type within the brain meninges, and recent studies have demonstrated the diverse ontogeny, transcriptomic profiles, and immune functions of meningeal macrophages at steady state [5, 8-12] and in several neuropathological conditions [8, 13-16].

Cytoplasmic calcium ($Ca^{2+}$) signaling underlies a wide variety of cellular homeostatic and inflammatory processes in macrophages [17-23]. In addition to intracellular $Ca^{2+}$ elevation, distinct spatiotemporal dynamics - including oscillation patterns, intracellular propagations, and intercellular synchronization of $Ca^{2+}$ signals - may regulate different macrophage functions during steady state and pathophysiology [20-25]. Despite our increased understanding of the diverse molecular signatures and contributions of meningeal macrophages to homeostasis and neuroinflammation, virtually nothing is known about their $Ca^{2+}$ signaling heterogeneity in both healthy and diseased states.

To comprehensively characterize the $Ca^{2+}$ dynamics of individual macrophages localized to the brain meninges, we combined intravital two-photon $Ca^{2+}$ imaging in a novel reporter mouse line, in which the $Ca^{2+}$ reporter GCaMP6s is expressed in platelet factor 4 ($Pf4^{+}$) meningeal macrophages, with an event-based signaling analysis pipeline. Our data reveal several distinct spatiotemporal $Ca^{2+}$ dynamic features in perivascular versus non-perivascular meningeal macrophages, including a unique coupling between the $Ca^{2+}$ signals of dural perivascular macrophages and behaviorally-driven vasomotion of their associated dural vessels at steady state. Furthermore, our data uncover both increases and decreases in $Ca^{2+}$ activity in distinct subsets of meningeal macrophages in response to cortical spreading depolarization (CSD), a pathophysiological brain hyperexcitability event linked to neuroinflammation [26] in migraine, traumatic brain injury, and stroke [27]. Mechanistically, our data suggest the calcitonin gene-related peptide/receptor activity-modifying protein 1 (CGRP/RAMP1) axis uniquely mediates CSD-evoked macrophage $Ca^{2+}$ elevation, indicating a brain-to-meninges neuroimmune signaling pathway involving the activation of meningeal peptidergic sensory neurons.

# Results

## Characterizing macrophage $Ca^{2+}$ signaling features in homeostatic brain meninges

Previous intravital imaging studies exploring the spatiotemporal dynamics of tissue-resident macrophages have primarily used CX3C motif chemokine receptor 1 (CX3CR1)-based mouse reporter strains [13, 22, 28, 29]. However, other resident monocyte-derived cells are labeled in these reporter mice [30, 31]. Moreover, brain microglia also express

46 CX3CR1 [13, 31-33], limiting the use of these reporter mice for resolving the
47 spatiotemporal subcellular $Ca^{2+}$ dynamics of macrophages localized to the relatively thin
48 meningeal layers covering the brain parenchyma. To systematically characterize
49 meningeal macrophage $Ca^{2+}$ dynamics *in vivo* and avoid contamination from $Ca^{2+}$ signals
50 arising from other resident monocyte-derived meningeal cells and superficial
51 parenchymal microglia, we leveraged recent findings showing the expression of Pf4 in
52 meningeal macrophages but not in parenchymal microglia, [10, 16, 34], and generated
53 transgenic reporter mice expressing the highly sensitive $Ca^{2+}$ indicator GCaMP6s (using
54 TIGRE2.0-based Ai162D mice [35]) in $Pf4^{+}$ macrophages (using $Pf4^{Cre}$ mice [36]).
55 Notably, nearly 100% of meningeal macrophages are labelled in $Pf4^{Cre}$-based reporter
56 mice [34]. Although Pf4 is also expressed by megakaryocytes [36], these cells are absent
57 in the brain meninges [5].
58
59 Anesthetic agents impact intracellular $Ca^{2+}$ signaling, including in brain macrophages and
60 other non-excitable glial cells [37-39]. We therefore investigated subcellular $Ca^{2+}$ activity
61 of meningeal macrophages in awake, behaving mice. We imaged meningeal
62 macrophages via a chronic cranial window implanted together with a restraining headpost
63 over the intact dura mater overlying the posterior neocortex. This chronic window
64 approach produces minimal inflammatory responses in the cortex and meninges below
65 the window [40, 41]. After at least 7 days of recovery, mice were gradually habituated
66 across multiple days to head restraint while free to run on a wheel (**Fig 1b**). We tracked
67 $Ca^{2+}$ transients of GCaMP6s-labeled meningeal macrophages using high-speed two-
68 photon microscopy in 37 fields of view (FOVs) from 7 mice. We first corrected the imaging

movies for locomotion-evoked meningeal translational shifts using rigid registration [41]. Movies were then processed using the AQuA2 data analysis platform [42], which implements an unbiased event-based approach to capture spatiotemporal $Ca^{2+}$ event dynamics (**Fig 1C**). Based on spatial analysis, we assigned events (n=1361), with their corresponding $Ca^{2+}$ features, to a given macrophage, with data gathered from a total of 503 cells.

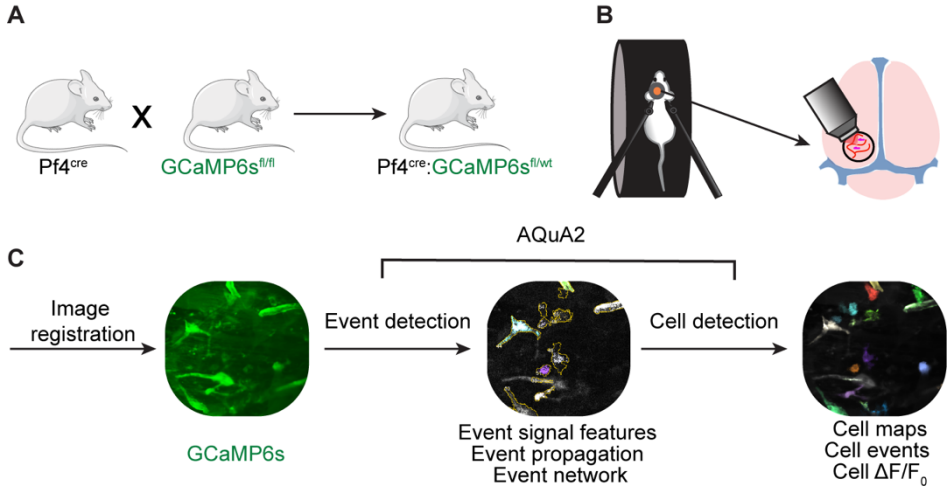


**Figure 1. Imaging meningeal macrophage $Ca^{2+}$ dynamics in awake behaving mice. (A)** $Pf4^{Cre}$:$GCaMP6s^{fl/wt}$ reporter mouse construct for imaging meningeal macrophages $Ca^{2+}$ activity. **(B)** Experimental procedure for two-photon imaging of meningeal macrophage $Ca^{2+}$ activity. Following the implantation of a headpost and a cranial window, mice were habituated to head restraint and subjected to two-photon microscopy while head-fixed on a running wheel to study meningeal macrophage $Ca^{2+}$ activity. **(C)** Macrophage $Ca^{2+}$ imaging processing pipeline.

We characterized $Ca^{2+}$ dynamics in two anatomically distinct macrophage populations: perivascular and interstitial non-perivascular (n=122; n=381, respectively, **Fig 2A and Video S1**). The vast majority of perivascular macrophages (93.4%, n=114) displaying ongoing $Ca^{2+}$ activity were associated with vessels in the dura mater. The two meningeal macrophage subpopulations exhibited several distinct $Ca^{2+}$ activity features. While the total area of $Ca^{2+}$ activity in the peri- and non-perivascular macrophages was similar (**Fig 2B**), the signal perimeter of perivascular

macrophages was significantly higher (**Fig 2C**) and exhibited a more elongated shape (**Fig 2A, 2D**). The $Ca^{2+}$ event duration in the perivascular macrophages was also longer compared to the non-perivascular subpopulation (**Fig 2F**). The peak $Ca^{2+}$ activity level (Max $DF/F_0$, **Fig 2E**) and event rate (**Fig 2G**), nonetheless, were similar in the two meningeal macrophage subpopulations.

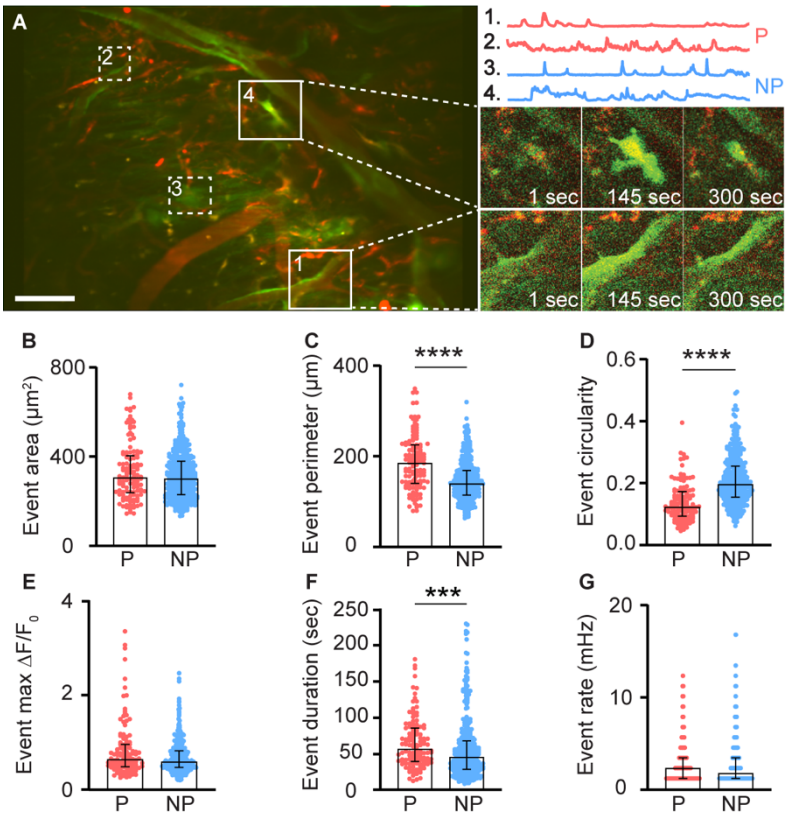


**Figure 2. $Ca^{2+}$ dynamic features of meningeal macrophages at steady state. (A)** Left: Mean projection of an example FOV depicting perivascular (P, red; 1, 2) and non-perivascular (NP, blue; 3, 4) meningeal macrophages (white squares). Scale bar 50 μm. Right: Corresponding macrophages with representative 900-second $Ca^{2+}$ activity traces (top) and their fluorescence signal at selected time points (bottom). **(B-G)** AQuA2-based morphological and $Ca^{2+}$ event functional features of perivascular (P=122 cells) and non-perivascular (NP, n=381 cells) meningeal macrophage. (B) Event area, (C) Event perimeter, (D) Event circularity, (E) Event max $DF/F_0$, (F) Event duration, (G) Event rate. Data (B-G) represent median ± IQR. ***p<0.001, ****p<0.0001, Mann-Whitney U-test. n=37 fields of view (FOVs) from 7 mice.

Distinct $Ca^{2+}$ signal frequency spectra may underlie different biological functions of macrophages [22]. We therefore analyzed meningeal macrophage $Ca^{2+}$ signal waveforms by performing a multi-step signal processing and clustering analysis. We clustered cells

108 based on two distinct patterns of $Ca^{2+}$ activity. Cells in Cluster 1 (n=40) exhibited a more
109 noisy-like activity pattern characterized by multiple frequencies, while cells in Cluster 2
110 (n=463) displayed a single dominant frequency at 0.01 Hz (**Fig 3A**). To further explore
111 these cellular signaling differences, we combined the clustering data with AQuA2-derived
112 features and observed that macrophages in Cluster 1 showed a larger event perimeter
113 and lower circularity and peak magnitude compared to those in Cluster 2 (**Fig 3D-F**).
114 Cluster 1 cells also had a lower signal-to-noise ratio compared to Cluster 2 cells (**Fig 3I**),
115 but had differences in terms of event area, duration, or rate (Figures 3C, G, H). There
116 was a significant association between cell cluster (1 vs. 2) and cell type, with Cluster 1
117 predominantly comprised of perivascular macrophages, and Cluster 2 including primarily
118 non-perivascular macrophages (**Fig 3J**), further indicating that these two meningeal
119 macrophage subpopulations have distinct $Ca^{2+}$ signaling properties.
120
121
122

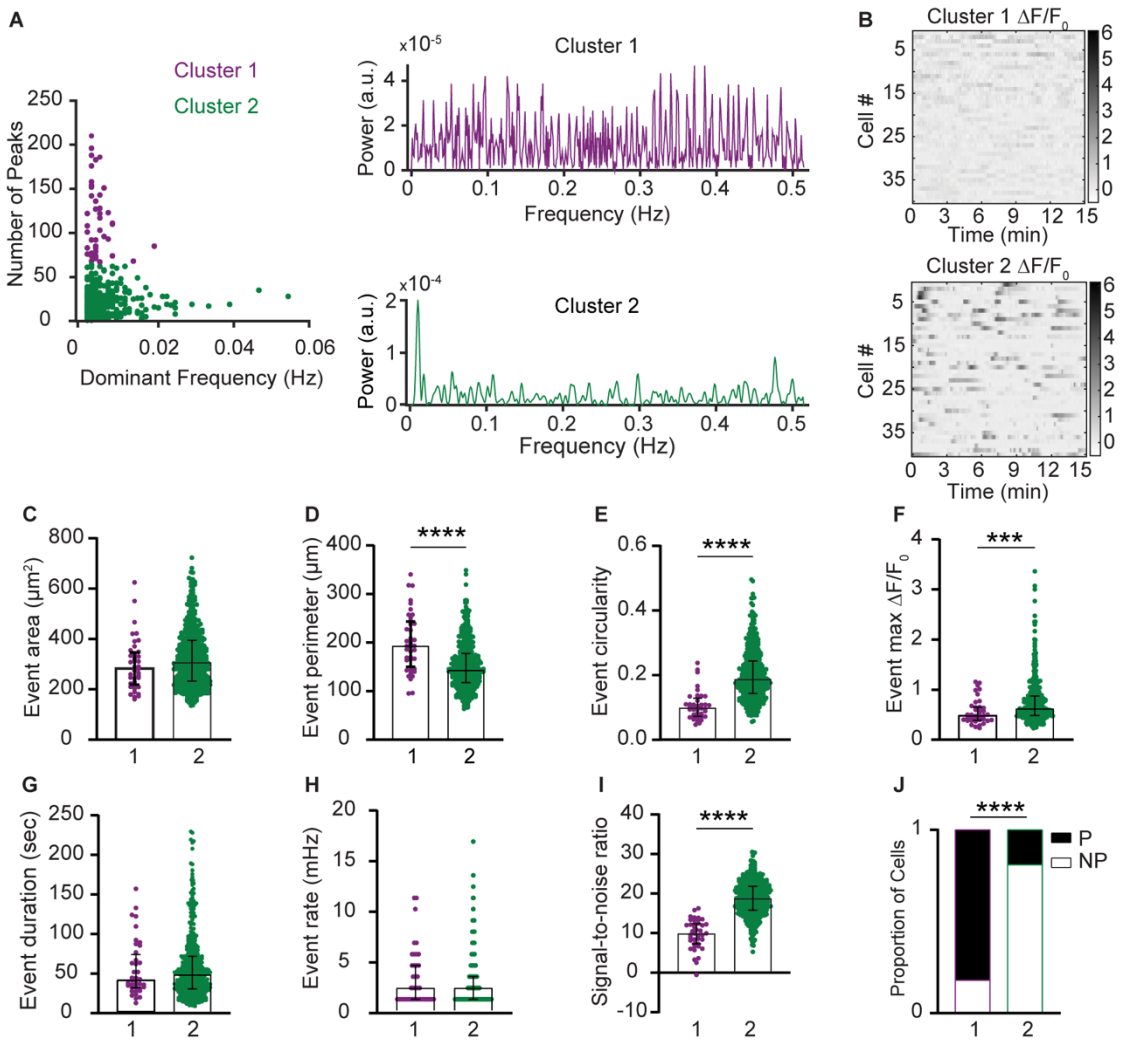


**Figure 3. Intracellular $Ca^{2+}$ signal frequency spectra of macrophage subsets in the steady-state meninges (A)** Left: Clustering of meningeal macrophage $Ca^{2+}$ activity based on frequency-domain features and peak detection. Cluster 1 (purple, n=40) and Cluster 2 (green, n=463). Right: Power spectrum density (PSD) of $Ca^{2+}$ signals for each cluster. **(B)** Example $DF/F_0$ heatmaps of Cluster 1 and Cluster 2 macrophages. **(C-H)** Morphological and $Ca^{2+}$ functional features of Cluster 1 and Cluster 2 macrophages. (C) Event area. (D) Event perimeter (E) Event circularity. (F) Event max $DF/F_0$. (G) Event duration. (H) Event rate. (I) Signal-to-noise ratio from Clusters 1 and 2**.** (J) Distribution of cell types across clusters. Data (C-I) represents median ± IQR. ***p<0.001, ****p < 0.0001, Mann-Whitney U-test Data (J) represents the cell proportion. ****p<0.0001, Chi-square test.

Intracellular $Ca^{2+}$ signal propagation underlies diverse cellular functions and has been recently identified in macrophages *in vitro* [21] and in skin-resident macrophages *in vivo* [43]. By assessing the $Ca^{2+}$ signal propagation maps of each event within a determined cell, we identified two distinct patterns of activity: propagating events in which $Ca^{2+}$ signals

139 traveled throughout the entire cell, and stationary events (**Fig 4A**). Propagating events
140 had varied signal source regions and directionality. Most macrophages (perivascular,
141 94.3%, n=115; non-perivascular, 86.9%, n=331) exhibited only propagating events, while
142 a small minority of cells displayed a mix of propagating and stationary events or
143 exclusively stationary activity events (**Fig 4B**).
144
145 Macrophage intercellular communication, including synchronized activity, potentially
146 across connected macrophage networks, has been implicated in maintaining tissue
147 homeostasis and immune function [18, 21, 44, 45]. To investigate meningeal macrophage
148 intercellular interactions, we characterized spatiotemporal relationships between $Ca^{2+}$
149 events in distinct cells within each FOV. We compared temporal factors, including the
150 relative onset latency ($t0_A$ – $t0_B$) between different macrophages and the duration of the
151 first occurring event ($t1_A$ – $t0_A$) (**Fig 4C**). We also compared the distances between
152 macrophage pairs exhibiting concurrent events and the number of synchronous events
153 (**Fig 4D**). Finally, we calculated the proportion of perivascular and non-perivascular
154 macrophages exhibiting synchronous $Ca^{2+}$ events. Across all FOVs, nearly half of the
155 macrophages (49.3%) exhibited synchronous $Ca^{2+}$ activity, involving cells at a wide range
156 of distances (**Fig 4E**), suggesting that spatial proximity does not influence event
157 synchronicity. Interestingly, there was poor correlation between the distance of cell pairs
158 exhibiting synchronous events and their timing (**Fig 4F**), suggesting that an external
159 factor, rather than intercellular coordinated networked activity, mediates this intercellular
160 signaling. When comparing synchronous activity among peri- and non-perivascular

macrophages, most cells exhibited mixed interactions between the same and different subtypes (**Fig 4G**).

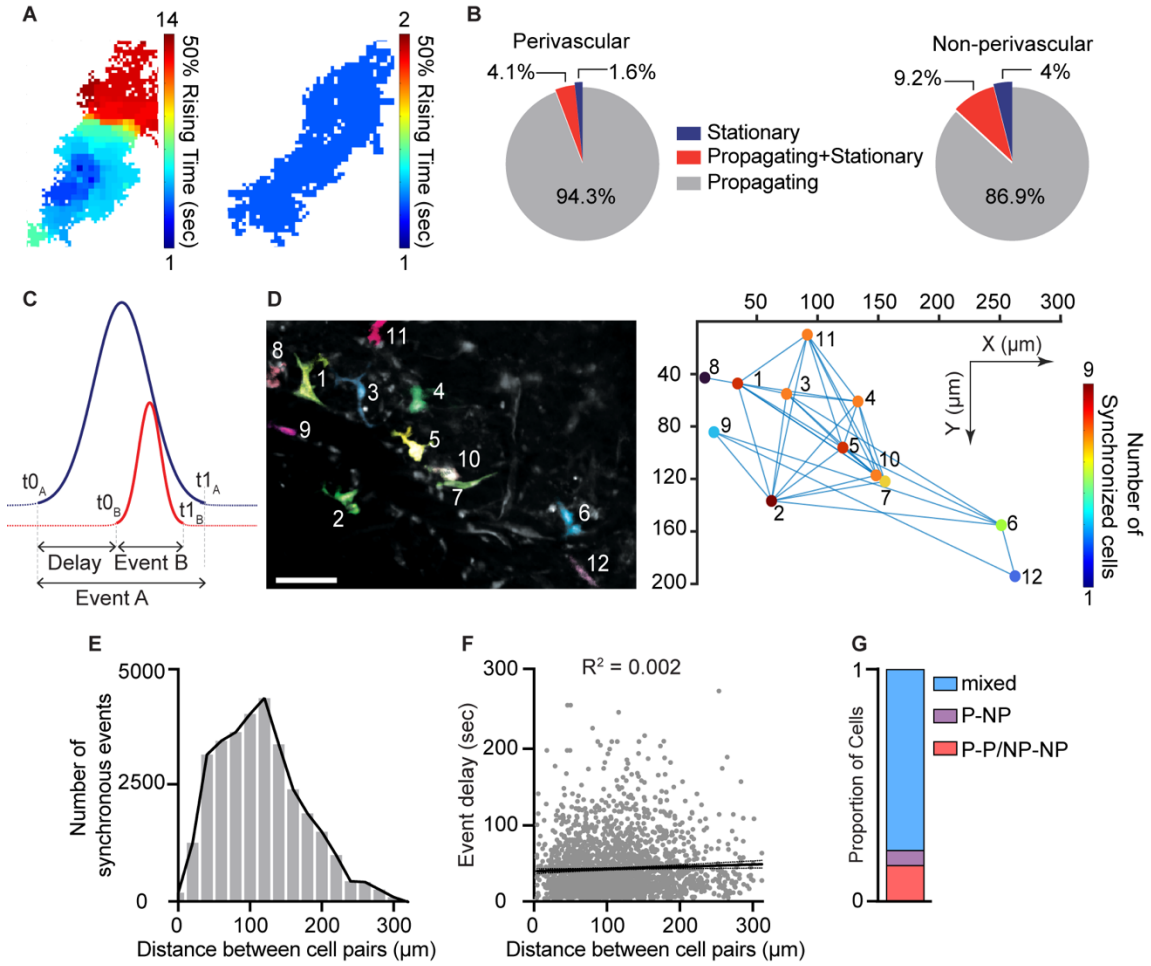


**Figure 4. Intracellular propagation and intercellular synchronization of meningeal macrophage $Ca^{2+}$ activity**. **(A)** Spatial maps of two distinct $Ca^{2+}$ events. Left: Propagating $Ca^{2+}$ activity. Right: Stationary $Ca^{2+}$ activity. **(B)** Distribution of event propagation profiles in perivascular and non-perivascular meningeal macrophages. **(C)** Schematic analysis paradigm for detecting synchronous $Ca^{2+}$ activity in meningeal macrophages. **(D)** Synchronous $Ca^{2+}$ events among meningeal macrophages within a FOV. Left: Mean projection of an example FOV showing $Ca^{2+}$ activity in distinct macrophages (colored/numbered). Scale bar 50 μm. Right: Spatial map of macrophages exhibiting synchronous $Ca^{2+}$ activity. Lines connect macrophages with synchronized $Ca^{2+}$ activity, and colors indicate the extent of $Ca^{2+}$ event synchronization. **(E)** Distribution of distances across macrophage pairs showing different numbers of synchronous $Ca^{2+}$ events. **(F)** Linear regression showing poor correlation between distances of macrophage with synchronized $Ca^{2+}$ activity and event delay. **(G)** Proportion of macrophages exhibiting a specific synchronized interaction (cells interacting only with the same subtype: P-P/NP-NP; cells interacting only with a different subtype: P-NP; mixed (cells interacting with the same and different subtypes).

179 **Dural perivascular macrophage $Ca^{2+}$ activity is tuned to behaviorally-**
180 **driven dural vasomotion**

181 Brain border macrophages in the leptomeninges and related parenchymal perivascular
182 spaces regulate pial arterial vasomotion indirectly by affecting vessel stiffness [6]. Yet,
183 interaction between vascular-associated macrophages residing in the dura mater, the
184 outermost meningeal layer, and dural vasomotion remains unknown. We employed a
185 Generalized Linear Model (GLM) approach to investigate functional interaction between
186 dural perivascular macrophage $Ca^{2+}$ signals and behaviorally-driven dural vessel
187 dynamics (**Fig 5A**). Dural arteries constrict during locomotion, while pial arteries dilate
188 [46]. We analyzed the locomotion-associated responses of 86 meningeal vessels (32
189 FOVs from 5 mice) and identified a subset (22%, n=19), whereby the diameter changes
190 were well fit by a GLM using the locomotion state as a predictor. Of these, we identified
191 74% (n=14) as dural vessels based on their GLM's negative coefficients consistent with
192 constriction (**Fig 5B and 5C**). Next, we fitted the $Ca^{2+}$ signal observed in perivascular
193 macrophages associated with these dural vessels (n=35) to a GLM using the diameter
194 changes as a predictor variable. Overall, the $Ca^{2+}$ activity of 83% (n=29) of these dural
195 macrophages was well predicted by the model (average deviance explained across all
196 well-fit macrophages: 0.43±0.15, mean±SD). Analysis of the macrophage-vascular
197 models' beta coefficients revealed two distinct interactions. About half of the
198 macrophages (55%, n=16) exhibited negative coefficients (i.e., increase and decrease in
199 $Ca^{2+}$ activity associated with dural vasoconstriction and recovery, respectively; **Fig 5B**
200 **and 5D**). The remaining macrophages (45%, n=13) exhibited positive coefficients (i.e.,
201 decrease and increase in $Ca^{2+}$ activity in response to dural constriction and recovery,

respectively; **Fig 5B and 5 E**). The coefficients for increased and decreased macrophage $Ca^{2+}$ activity peaked near zero delay relative to the vasoconstriction and were not statistically different (**Fig 5D-E and 5H**). These data provide evidence that dural perivascular macrophages are functionally coupled to dural vasomotion, either responding to or mediating such behaviorally driven vascular response.

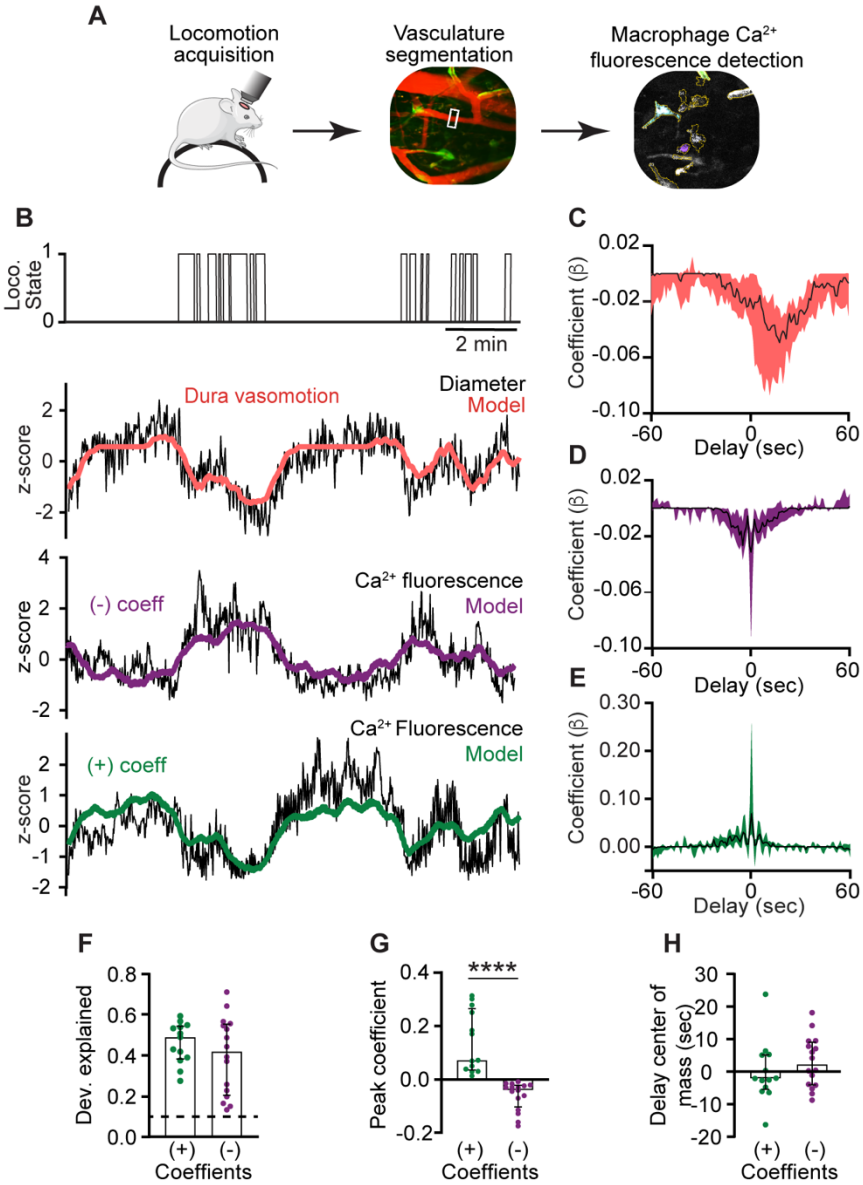


**Figure 5. $Ca^{2+}$ signals of dural perivascular macrophages are functionally coupled to behaviorally driven dural vasomotion. (A)** Experimental paradigm: Locomotion data were acquired during imaging in awake-behaving mice. Behaviorally-evoked changes in meningeal vessel diameter were obtained using segmentation of vessels labeled with a tracer during

macrophage $Ca^{2+}$ and further tested for coupling with $Ca^{2+}$ signals. **(B)** Example data of macrophages with $Ca^{2+}$ activity tuned to locomotion-related dural vessel vasomotion. Locomotion bouts (top trace) and dural vessel diameter (black trace) that was well fit by a GLM (red line) using locomotion state as a predictor. Note vasoconstriction during locomotion, indicating a dural vessel. The two bottom traces depict the $Ca^{2+}$ signal (black traces) of distinct meningeal macrophages that were well-fit by a GLM using dural vessel diameter as a predictor, showing either a negative coefficient (purple) or a positive coefficient (green). **(C)** Temporal profile of dura vessels GLM coefficients averaged across all well-fitted vessels (n=19). Traces represent the median across all well-fit ROIs, with shaded regions indicating IQR. **(D, E)** Temporal profiles of GLM coefficient values for macrophages' $Ca^{2+}$ activity averaged across all well-fitted cells (purple, negative coefficient, n=16; green, positive coefficient, n=13). Traces represent the median across all well-fit macrophages, with shaded regions indicating IQR. **(F)** The deviance explained (goodness-of-fit estimates) of the vessel diameter data included in the GLM used to predict macrophage $Ca^{2+}$ activity were not statistically different for macrophages showing negative (n=16) and positive (n=13) coefficients, suggesting similar interaction levels. **(G)** Comparison of peak positive and negative coefficients of well-fit macrophage $Ca^{2+}$ activity/vasomotion GLMs. **(H)** Center of mass of GLM coefficients indicating that dural vessel diameter changes drive bidirectional changes in fluorescence signal at zero delay. Data (F-H) are median ± IQR. ****$p<0.0001$ (Mann-Whitney U-test).

## An acute aberrant pro-inflammatory brain hyperexcitability event drives diverse $Ca^{2+}$ dynamics in meningeal macrophages

CSD is an aberrant brain hyperexcitability event linked to parenchymal inflammation and pain in migraine, traumatic brain injury, and stroke [27, 47, 48], and could also affect meningeal macrophages [49]. In anesthetized mice subjected to an acute CSD episode, a small subset of meningeal macrophages undergoes morphological changes resembling an inflammatory state [26]. Given the direct anatomical and functional connection between the brain and meninges [11, 50] and the involvement of intracellular $Ca^{2+}$ influx in macrophage inflammatory activation [51], we asked whether brain-to-meninges signaling drives intracellular $Ca^{2+}$ elevations in meningeal macrophages in the wake of CSD. We therefore triggered a single CSD episode in the frontal cortex [52, 53] and characterized the related changes in meningeal macrophage $Ca^{2+}$ dynamics. In each experiment, we verified CSD induction based on the associated acute meningeal

245 deformation and/or pial vasoconstriction observed in awake animals ([53] and **Video S2**).
246 We studied CSD-related $Ca^{2+}$ dynamics in 249 macrophages (perivascular, n=64; non-
247 perivascular, n=185; 13 FOVs from 10 mice). For each cell, we compared $Ca^{2+}$ event
248 rates during the passage of the CSD wave (1 min) and the PostCSD period (30 min) to
249 baseline (PreCSD, 30 min) to assess acute and persistent $Ca^{2+}$ responses, respectively.
250 We characterized cells as exhibiting persistently increased (event rate > 2× PreCSD),
251 decreased (event rate < 0.5× PreCSD), or unchanged responses. Given the low $Ca^{2+}$
252 activity rate observed under steady state and the likelihood that no spontaneous $Ca^{2+}$
253 elevations occur during the brief period of the CSD event, we considered cells to be either
254 acutely activated or exhibiting an unchanged $Ca^{2+}$ response. CSD evoked both acute and
255 persistent $Ca^{2+}$ activity changes in (**Fig 6 A-E and Video S2**). While smaller subsets of
256 meningeal macrophages exhibited acute (21.3%, n=53) and/or persistent increase
257 (22.1%, n=55) in their $Ca^{2+}$ activity, the majority of cells (58.6%, n=146) exhibited a
258 persistent decrease. An acute increase was observed more often in peri- vs non-
259 perivascular macrophages (perivascular, 32.8%, n=21; non-perivascular, 17.3%, n=32,
260 **Fig 6F**). Persistent changes in $Ca^{2+}$ activity were observed similarly in peri- and non-
261 perivascular macrophages (increases; perivascular, 28.2%, n=18; non-perivascular,
262 18.4%, n=37; decreases; perivascular, 50.0%, n=32; non-perivascular, 61.6%, n=114,
263 **Fig 6G**). The macrophages' propensity to develop a persistent $Ca^{2+}$ increase was
264 unrelated to their acute response (**Fig 6H**), suggesting that the mechanisms underlying
265 these two temporal responses are distinct. However, cells showing no acute activation
266 were more likely to display decreased $Ca^{2+}$ activity post-CSD (**Fig 6H**). Finally, we
267 observed that macrophages exhibiting a persistent increase in $Ca^{2+}$ activity had a lower

268 baseline activity when compared to cells showing a persistent (**Fig 6I**), suggesting that

269 this post-CSD response is influenced by the macrophages' basal response activity.

270

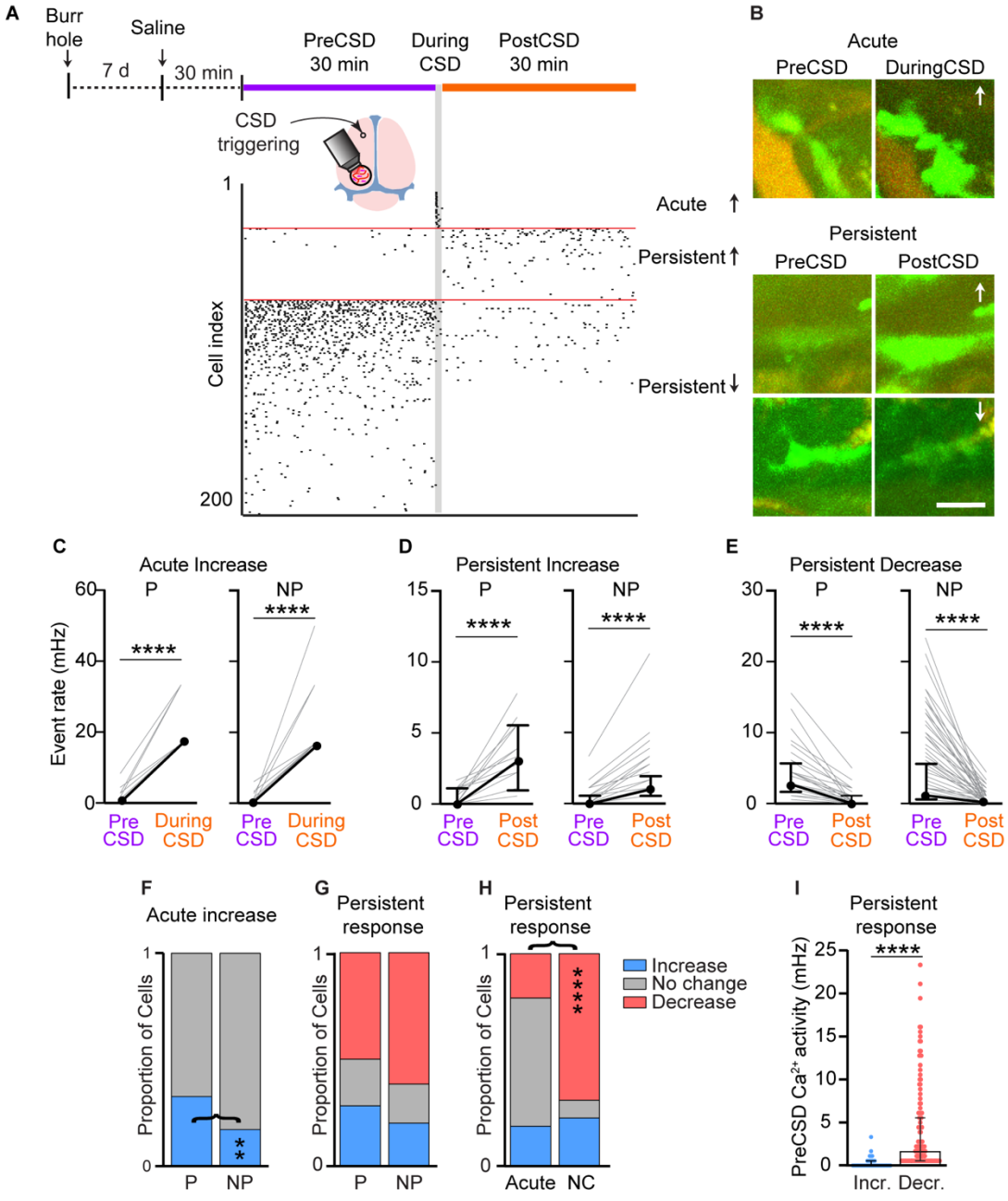


271

272 **Figure 6. Diverse meningeal macrophage $Ca^{2+}$ dynamics following cortical spreading**
273 **depression (CSD). (A)** Experimental setup and example data: (top) A small burr hole was drilled
274 above the frontal cortex 7 days before $Ca^{2+}$ imaging. Mice were pretreated with saline 30 min
275 before imaging baseline macrophage $Ca^{2+}$ activity (30 min, PreCSD). CSD was then induced with
276 a pin prick, and macrophage $Ca^{2+}$ activity was assessed during CSD (1 min during CSD), and

post-CSD (30 min, post-CSD). (Bottom) A raster plot of macrophage $Ca^{2+}$ activity showing the acute and persistent increases and persistent decrease in response to CSD. **(B)** Example of macrophage $Ca^{2+}$ fluorescence changes following CSD. Images depict the mean projection over the specific experimental timeline. Arrows indicate an increase or a decrease in $Ca^{2+}$ activity. Scale bar 50 µm. **(C)** Individual responses of perivascular (P, n=21) and non-perivascular (NP, n=32) macrophages showing an acute increase in $Ca^{2+}$ activity. **(D)** Individual response of P (n=18) and NP (n=37) macrophages exhibiting a persistent increase in $Ca^{2+}$ activity. **(E)** Individual responses of P (n=32) and NP (n=114) macrophages showing a persistent decrease in $Ca^{2+}$ activity. **(F)** Proportion of P and NP macrophages showing an acute increase in $Ca^{2+}$ activity or no acute change. **(G)** Proportion of P and NP macrophages showing a persistent increase, decrease, or no change in $Ca^{2+}$ activity. **(H)** Proportion of macrophages displaying distinct persistent responses stratified based on their acute response. **(I)** Baseline (PreCSD) $Ca^{2+}$ activity in macrophages exhibiting persistent increased (n=55) or decreased activity (n=146). Data (C-E) are median ± IQR. ****p<0.0001 (Wilcoxon signed rank test). Data (F-H) represents the proportion of cells, **p<0.01; ****p<0.0001 (Chi-square test). Data (I) are median ± IQR. ****p<0.0001 (Mann-Whitney U-test).

## CGRP/RAMP1 signaling mediates CSD-evoked persistent increase in meningeal macrophage $Ca^{2+}$ activity

Many meningeal macrophages are localized near peptidergic sensory axons [16]. In the wake of CSD, cortex-to-meninges signaling enhances the responsiveness of meningeal sensory neurons and can drive the release of the neuropeptide CGRP from their peripheral nerve endings [52-54]. CGRP-expressing sensory neurons regulate tissue immunity, including meningeal macrophage function, via the CGRP/RAMP1 neuroimmune axis [16, 55]. We therefore asked whether the CSD-related changes in meningeal macrophage $Ca^{2+}$ dynamics we observed involve CGRP/RAMP1 signaling. We pretreated mice with the RAMP1 antagonist BIBN4096 and then imaged meningeal macrophage $Ca^{2+}$ activity (42 cells; perivascular, n=14; non-perivascular, n=28; 3 FOVs from 3 mice) before and after CSD. As expected, RAMP1 blockade did not affect CSD triggering [56]. When compared to control saline treatment, RAMP1 blockade also did not reduce basal macrophage $Ca^{2+}$ activity (**Fig 7B**). Blocking CGRP/RAMP1 signaling neither affected the incidence of acute increases in $Ca^{2+}$ activity (**Fig 7A and 7C**) nor the

309 magnitude of that response (**Fig 7D**). RAMP1 antagonism, however, inhibited the CSD-
310 evoked persistent increase in the macrophage's $Ca^{2+}$ activity, without affecting the
311 incidence of the persistent decrease (**Fig 7E**). The data suggest that in the wake of CSD,
312 the CGRP/RAMP1 axis, likely involving a peripheral sensory neuroimmune signaling, is
313 responsible for the prolonged enhancement of $Ca^{2+}$ signaling in a subset of meningeal
314 macrophages, which could potentially mediate their pro-inflammatory response.
315

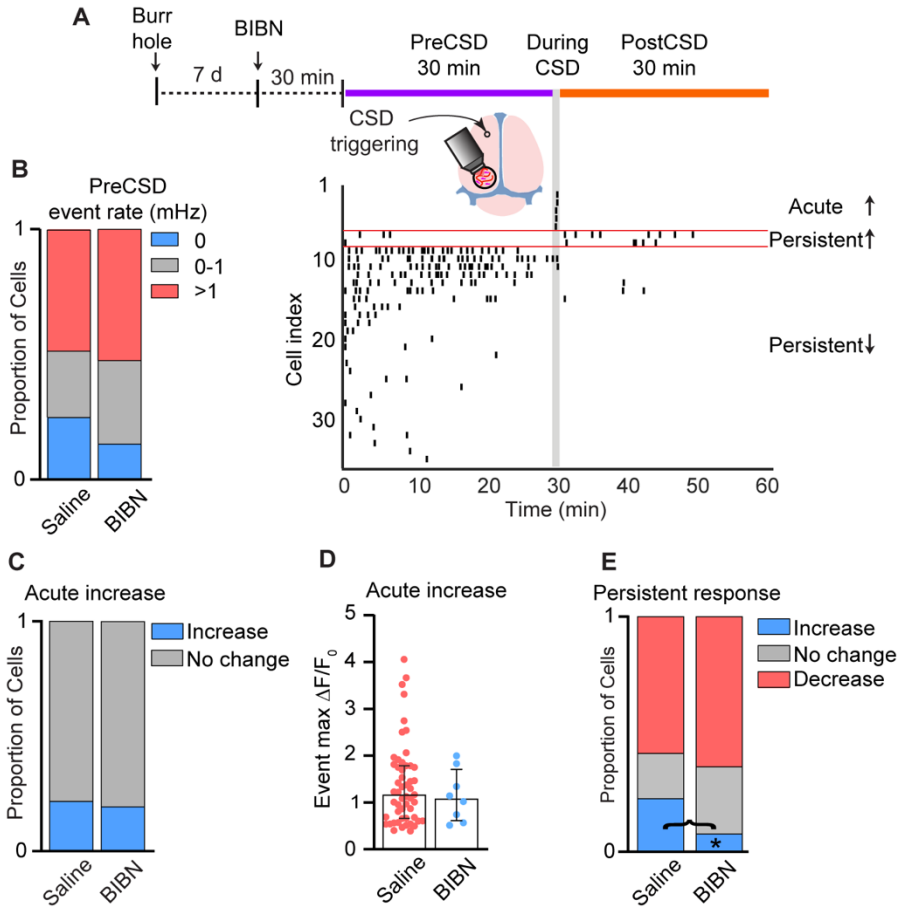

316

317 **Figure 7. CGRP/RAMP1 signaling mediates CSD-related persistent increase in meningeal**
318 **macrophage $Ca^{2+}$ activity. (A)** Experimental setup and example data: (top) A small burr hole
319 was drilled above the frontal cortex 7 days before $Ca^{2+}$ imaging. Mice were pretreated with the
320 RAMP1 antagonist BIBN4096 (BIBN) 30 min before imaging baseline macrophage $Ca^{2+}$ activity
321 (30 min, PreCSD). CSD was then induced with a pin prick, and macrophage $Ca^{2+}$ activity was
322 assessed during CSD (1 min during CSD), and post-CSD (30 min, post-CSD). (Bottom) A raster
323 plot of macrophage $Ca^{2+}$ activity showing the acute and persistent increases and persistent

decrease in response to CSD. **(B)** RAMP1 inhibition does not affect the baseline (PreCSD) event rate. Data compared between macrophages imaged in saline-treated mice (n=249 cells) and BIBN-treated mice (n=42 cells). **(C)** RAMP1 antagonism does not affect the CSD-evoked acute increase in macrophage $Ca^{2+}$. Proportion of macrophages showing an acute response (increase vs. no change) in saline-treated mice (n=249 cells) and BIBN-treated mice (n=42 cells). **(D)** RAMP1 antagonism does not affect the magnitude of the acute macrophage $Ca^{2+}$ signal. Event max $DF/F_0$ in macrophages showing an acute $Ca^{2+}$ increase in saline-treated mice (n=53 cells) and BIBN-treated mice (n=8 cells). **(E)** RAMP1 antagonism distinctly inhibits the persistent increase in macrophage $Ca^{2+}$ activity post CSD. Proportion of macrophages showing persistent increase, persistent decrease, or no persistent change in saline-treated mice (n=249 cells) and BIBN-treated mice (n=42 cells). **(F)** Data (B, C, E) represents the proportion of cells. *$p<0.05$, Fisher's exact test. Data (D) are median ± IQR.

# Discussion

Resident macrophages in the brain meninges are essential for maintaining brain homeostasis, regulating central nervous system immune surveillance, and mediating neuroimmune responses under pathological conditions [12, 14, 16, 57-59]. Macrophages rely on $Ca^{2+}$ signaling to mediate many of their functions [17-23]. Here, using two-photon microscopy in awake, behaving $Pf4^{Cre}$:GCaMP6s reporter mice, we describe the heterogeneity of meningeal macrophage $Ca^{2+}$ dynamics at steady state and in response to CSD, an aberrant cortical hyperexcitability event associated with migraine, traumatic brain injury, and stroke. Our data suggest the presence of two subsets of macrophages in discrete meningeal niches, perivascular and non-perivascular, that exhibit several distinct $Ca^{2+}$ signal properties at steady state. We further demonstrate $Ca^{2+}$ activity in dural perivascular macrophages tuned to behaviorally-driven dural vasomotion. Finally, we describe opposing $Ca^{2+}$ responses of meningeal macrophages following CSD, and demonstrate the contribution of the CGRP/RAMP1 axis in mediating CSD-evoked persistent $Ca^{2+}$ elevations.

353 The exact link between the distinct $Ca^{2+}$ signal properties of meningeal macrophage
354 subsets observed herein and their homeostatic function remains to be established. The
355 lower event magnitude and noisier signal observed in dural perivascular macrophages
356 may reflect functional interactions with the pulsation dynamics of dural vessels [46].
357 Indeed, by combining vascular and macrophage $Ca^{2+}$ imaging, we demonstrate a tight
358 temporal association between the diameter fluctuations of the dural vessels and the $Ca^{2+}$
359 signal of their associated macrophages in awake, locomoting mice. Direct vascular-
360 macrophage coupling may underlie this interaction, involving macrophages sensing
361 vascular-related mechanical changes via Piezo1 signaling [60]. Functional vascular-
362 macrophage interaction may also involve mural cells as inter-mediators [58, 61]. Studying
363 whether macrophage $Ca^{2+}$ signaling regulates dural vasomotion will require an
364 experimental approach that has yet to be developed, allowing for their selective
365 manipulation. The paucity of ongoing $Ca^{2+}$ activity in perivascular macrophages situated
366 in the leptomeninges we observed supports recent findings that subdural perivascular
367 macrophages indirectly affect pial and parenchymal vasomotion via extracellular matrix
368 remodeling [6].
369
370 Intracellular $Ca^{2+}$ signal propagation has been observed in various non-excitable cells,
371 such as astrocytes [62]. We show that the majority of meningeal macrophages, including
372 peri- and non-perivascular, exhibit intracellular $Ca^{2+}$ signals that propagate throughout the
373 entire cell, suggesting microdomain intracellular $Ca^{2+}$ signal elevation, following release
374 from internal stores. By characterizing the spatiotemporal relationships between $Ca^{2+}$
375 signals in distinct cells, we also demonstrate synchronous events that are independent of

spatial proximity, suggesting that synchronous $Ca^{2+}$ activity is not driven by intercellular communication but rather by an external signal. Interestingly, our data indicate that synchronized events involve both peri- and non-perivascular macrophages, despite having distinct $Ca^{2+}$ elevation features, suggesting that these meningeal macrophage subtypes similarly sense external signals.

Cortex-to-meninges signaling involves a relatively slow flow of soluble molecules in the cerebrospinal fluid reaching the subarachnoid space and advancing via arachnoid cuff exit points into the dura mater [11, 50]. Our finding of an acute $Ca^{2+}$ elevation in a subset of extrasinusoidal perivascular dural macrophages coinciding with the CSD event suggests a rapid transfer of soluble signaling factors from the cortex across all meningeal layers [47]. Nevertheless, we cannot exclude a mechanically driven macrophage response to the acute meningeal deformation produced by the neuronal and glial swelling and shrinkage of the cortical extracellular space during CSD [53, 63, 64]. Our data also indicate a delayed and prolonged increase in $Ca^{2+}$ signal in a relatively small subset of macrophages post-CSD, which could underlie their proinflammatory-like morphological change [49, 51]. Our findings also support the view that meningeal neuroimmune CGRP/RAMP1 axis serves as a mechanism responsible for this macrophage $Ca^{2+}$ response, likely via the activation of their CGRP receptors [16]. Whether the relatively small subset of meningeal macrophages featuring increased $Ca^{2+}$ signaling serves a protective role [65, 66] or a proinflammatory, destructive function [67] remains to be elucidated. Intriguingly, our data points to a persistent decrease in macrophage $Ca^{2+}$

activity post-CSD, not involving CGRP/RAMP1 signaling, as the most prevalent response, raising the possibility that a hyperexcitable cortex dampens meningeal immunity.

# Conclusions

We provide a detailed characterization of macrophage $Ca^{2+}$ dynamics in homeostatic meninges, thereby expanding our understanding of their biological diversity. The coupling of dural perivascular macrophage $Ca^{2+}$ signals and dural vasomotion may represent a unique homeostatic functional dural macrophage-vascular unit that controls dural perfusion. The diversity of meningeal macrophage $Ca^{2+}$ responses to CSD further highlights the complexity of brain-to-meninges neuroimmune signaling and meningeal macrophage function in neurological disorders such as migraine, traumatic brain injury, and stroke. Our study also provides essential genetic and data analysis tools to further understand the molecular signaling underlying macrophage function at steady state and neuropathological conditions.

# Methods

## Animals

All experimental procedures were approved by the Beth Israel Deaconess Medical Center Institutional Animal Care and Use Committee. Experiments were conducted on adult $Pf4^{Cre/wt}$:$TIGRE2.0^{GCaMP6s/wt}$ $Ca^{2+}$ reporter mice (8-17 weeks) (9 males, 5 females). Mice were generated by crossing $Pf4^{Cre}$ (C57BL/6-Tg (Pf4-icre) Q3Rsko/J, Jackson laboratory, Strain #008535) mice with $GCaMP6s^{fl/fl}$ (Ai162D; B6.Cg-$Igs7^{tm162.1(tetO-}$

420 GCaMP6s,CAG-tTA2)Hze/J, Jackson laboratory, Strain #031562) mice. Animals were
421 genotyped by Transnetyx Inc.
422

423 ## Surgical procedures

424 Animals were anesthetized using isoflurane in 100% $O_2$ (induction: 3%; maintenance:
425 1.5-2%) and placed on a heating pad with a rectal probe attached to a stereotaxic frame
426 to monitor animal body temperature during surgery. Animals received dexamethasone (8
427 mg/kg, i.p.) and Meloxicam SR (4 mg/kg, s.c.) to reduce inflammation and improve
428 surgical outcomes. An eye ointment was used to prevent ocular drying. Mice were
429 implanted with a titanium headpost and a 3 mm glass cranial window (1.5 mm lateral and
430 2 mm posterior to Bregma) over an intact dura covering the left posterior neocortex [53].
431 Immediately after surgery, the mouse cage was placed on a water-circulating heating pad
432 for faster recovery. Animals were then single-housed with access to a running wheel and
433 a hut and allowed to recover for at least one week.
434

435 ## Wheel running acclimation

436 After the cranial window surgery, mice were allowed to recover for at least a week. To
437 reduce stress associated with head-fixation during imaging and habituate to wheel
438 running, the mice received multiple training sessions (10 min to 1 h over 3–4 days). In
439 each session, the mouse was placed on a 3D printed running wheel, with its headpost
440 attached to two clamps, and allowed to locomote freely.
441

442 ## Two-photon $Ca^{2+}$ imaging

443 Awake-behaving mice were head-fixed to the running wheel by its headpost (**Figure 1**).
444 We used a two-photon microscope (Neurolabware) with a Nikon 16X, 0.8 NA objective to
445 acquire images at 15.5 Hz with digital zoom set at 4X (312 x 212 $\mu m^2$ FOV). A MaiTai
446 laser set to 920 nm with 25–40 mW power was used to excite fluorescence. The Scanbox
447 package for MATLAB (Neurolabware) was used to control the microscope and acquire
448 images and wheel running data. To image the meningeal vasculature, mice were
449 administered 70kDa TRITC-Dextran tracer (50 mg/kg, i.v.; Sigma-Aldrich).
450

451 **Behavioral tracking during two-photon imaging**

452 We recorded running speed in MATLAB using a custom-made encoder (Arduino) coupled
453 to the 3D-printed running wheel. See below for details of analyses of behavioral variables.
454

455 **Induction of CSD and pharmacological treatment**

456 For CSD induction, a 1 mm burr hole was drilled at the frontal bone (1.5 mm anterior to
457 the cranial window) to allow access to the brain cortical surface. A small amount of
458 silicone elastomer (Kwik-Cast, WPI) was placed to cover the burr hole opening, and the
459 animal was left to recover for at least one week. CSD was induced using a brief 2-second
460 cortical pinprick [53]. CSD induction was confirmed by the identification of a short-lasting
461 meningeal deformation and/or transient pial constriction [53]. On the experimental day,
462 30 minutes before baseline recording, mice were pretreated with the CGRP/RAMP1
463 antagonist BIBN4096 (0.3 ml, 1 mg/kg, i.p., Tocris) [54] or 0.3 ml of saline (Vehicle
464 control).
465

466 ## Quantification and statistical analysis

467

468 **Two-photon imaging movie processing**

469 We used a discrete Fourier transform to perform rigid registration to correct translation
470 changes due to brain motion during locomotion. Movies were then downsampled to 1.03
471 Hz. Locomotion signals were detected as described [41]. All image processing and
472 locomotion signal extraction were performed in MATLAB 2021b (Mathworks).

473

474 **$Ca^{2+}$ signal detection pipeline**

475 For detecting macrophage $Ca^{2+}$ signals, we used the Activity Quantification and Analysis
476 (AQuA2) platform that implements an event-based approach with advanced machine
477 learning techniques for temporal and spatial segmentation of $Ca^{2+}$ fluorescence events
478 [38]. Importantly, this computational platform captures event dynamics beyond traditional
479 ROI-based approaches. The following user-defined parameters were input: 0.49 μm/pixel
480 spatial resolution, 1.03 Hz temporal resolution, 1-second minimal event duration
481 detection; window of event size between 25% (125 $\mu m^2$/ 523 pixels) and 150% (750 $\mu m^2$/
482 3140 pixels). Every event and cell identified was followed by a manual visual check.
483 Subsequently, each cell was labelled as perivascular or non-perivascular according to its
484 location relative to vessels. Morphological features (area, perimeter, circularity) and
485 spatiotemporal aspects of the $Ca^{2+}$ signals (i.e., $\Delta F/F_0$ dynamics, frequency, amplitude,
486 duration) were used to analyze cell-specific characteristics and $Ca^{2+}$ activity profiles. We
487 employed the AQuA2 automatically-generated function [42] to characterize intracellular
488 $Ca^{2+}$ propagation. Intercellular $Ca^{2+}$ activity was evaluated by analyzing temporally co-

occurring events (synchronized event pairs), as well as their corresponding spatial localization in the FOV. All post-processing of AQuA2-generated data was performed using MATLAB 2021b (Mathworks).

**Clustering of $Ca^{2+}$ dynamics**

We used a Savitzky-Golay filter to detrend and smooth $Ca^{2+}$ activity traces. Polynomial order and frame size were optimized for each cell by selecting the combination of parameters that yielded a better signal-to-noise ratio. From the filtered signals, we extracted the dominant frequency using Fast Fourier Transform, and peak counts using minimum peak prominence (threshold of 10% signal amplitude range). The optimal number of clusters was determined using the Elbow method, after which k-means clustering was applied to group cells based on their signal characteristics.

**Analysis of CSD-related changes in macrophage $Ca^{2+}$ dynamics**

For analyzing the effects of CSD on macrophages' $Ca^{2+}$ dynamics, we divided the activity of each cell into three phases: 'PreCSD' (minutes 0 – 30), 'DuringCSD' (minutes 30 – 31), and 'PostCSD' (minutes 31 – 61). $Ca^{2+}$ event rate during CSD and PostCSD was compared against that of the PreCSD baseline for evaluation of acute and persistent $Ca^{2+}$ responses, respectively. $Ca^{2+}$ responses were categorized as increased (event rate > 2x PreCSD), decreased (event rate < 0.5x PreCSD), or unchanged.

**Analysis of locomotion**

512 We extracted running speed (cm/sec) from the wheel encoder. To infer the locomotion
513 state, we first concatenated all velocity signals obtained from a given mouse across all
514 experiments and trained a two-state Hidden Markov Model using the MATLAB function
515 'hmmtrain'. Then, the locomotion state was inferred for each individual imaging run by
516 applying the MATLAB function 'hmmviterbi' with the model trained on the concatenated
517 data. Locomotion bouts were defined as periods when the locomotion state was sustained
518 for at least two seconds.
519

520 **Vascular signals**

521 We calculated changes in vascular diameter by first generating a maximum intensity
522 projection of the red channel and drawing polygons (ROIs) around each vessel.
523 Subsequently, for each frame, pixels inside each ROI were extracted, and a Radon
524 transform was applied to get a 1D vessel profile. Radon transform of the first frame was
525 used as a reference to normalize the results of all subsequent frames, resulting in a time
526 series of normalized diameter traces.
527

528 **General linear models (GLM)**

529 We investigate the functional interaction between dural perivascular macrophage $Ca^{2+}$
530 activity and dural vasomotion by fitting a Gaussian GLMs using the GLMnet package
531 (MATLAB 2021b), with elastic net regularization (α=0.01) and ten-fold cross-
532 validation. We employed a two-step modeling. The first model was used to identify dural
533 vessels by evaluating the correlation of vessel diameter changes to locomotion state,
534 classifying dural or pial vessels according to their vasoconstriction and vasodilation

535 dynamics, respectively [46]. The second modeling step evaluated the relative contribution
536 of perivascular dural $Ca^{2+}$ activity signals to dural vessel diameter changes. All signals
537 were downsampled to 1.03 Hz to match the frame rate used when extracting fluorescence
538 $Ca^{2+}$ signals in AQuA2. To allow potential anticipatory or delayed responses of diameter-
539 to-locomotion or $Ca^{2+}$ fluorescence-to-diameter, the time interval used to analyze the
540 response to the predictor was set from -60 s to +60 s. The GLM was trained on 75% of
541 the data, and all predictions and model performances reported are from the remaining
542 25% testing set. A threshold of 0.1 goodness-of-fit deviance explained was set. For each
543 predictor temporal shift, a response coefficient was generated. Centroid delay between
544 predictor and response was calculated, weighted by the absolute value of the coefficient
545 (i.e., center-of-mass, COM).
546
547 **Statistical analysis**
548 All statistical analysis was performed using GraphPad Prism 10.4 and MATLAB 2021b.
549 Data were analyzed using a Wilcoxon matched-pairs signed rank sum test or a Mann-
550 Whitney U-test. Distribution of categorical data was analyzed using the Chi-square or
551 Fisher's exact test. P-values are indicated as follows: *$p<0.05$, **$p<0.01$, ***$p<0.001$,
552 ****$p<0.0001$.
553
554 **Data availability.**
555 All data needed to evaluate the conclusions in the paper are present in the paper.
556 The code used for analyzing the data in this study was deposited in the Levy Lab
557 GitHub account.

558 Code for movie processing is available at:

559 https://github.com/levylabheadache/MovieProcessing/tree/SCN;

560 Code for locomotion analysis is available at:

561 https://github.com/levylabheadache/Locomotion/tree/SCN;

562 Code for post Aqua2-processing is available at:

563 https://github.com/levylabheadache/Aqua2Processing;

564 Code for vascular segmentation is available at:

565 https://github.com/levylabheadache/Vasculature/tree/SCN;

566 Code for GLM is available at:

567 https://github.com/levylabheadache/GeneralLinearModel_Macrophages

568 Any additional information is available from the corresponding author upon request.

569

570 **Abbreviations**

571 AQuA2 – Activity Quantification and Analysis

572 $Ca^{2+}$ – Cytoplasmic calcium

573 CGRP – Calcitonin gene-related peptide

574 CSD – Cortical spreading depolarization (depression)

575 CX3CR1 – CX3C Motif chemokine receptor 1

576 GLM – General Linear Model

577 NP – Non-perivascular

578 P – Perivascular

579 Pf4 – Platelet factor 4

580 RAMP1 – Receptor activity modifying protein 1

TRITC – Tetramethylrhodamine isothiocyanate

# References


1. Okabe Y, Medzhitov R. Tissue biology perspective on macrophages. Nat Immunol. 2016;17(1):9-17. doi: 10.1038/ni.3320. PubMed PMID: 26681457.

2. Guilliams M, Thierry GR, Bonnardel J, Bajenoff M. Establishment and Maintenance of the Macrophage Niche. Immunity. 2020;52(3):434-51. doi: 10.1016/j.immuni.2020.02.015. PubMed PMID: 32187515.

3. Mass E, Nimmerjahn F, Kierdorf K, Schlitzer A. Tissue-specific macrophages: how they develop and choreograph tissue biology. Nature reviews. 2023;23(9):563-79. Epub 20230315. doi: 10.1038/s41577-023-00848-y. PubMed PMID: 36922638; PubMed Central PMCID: PMCPMC10017071.

4. Kierdorf K, Masuda T, Jordao MJC, Prinz M. Macrophages at CNS interfaces: ontogeny and function in health and disease. Nat Rev Neurosci. 2019;20(9):547-62. Epub 20190729. doi: 10.1038/s41583-019-0201-x. PubMed PMID: 31358892.

5. Rustenhoven J, Drieu A, Mamuladze T, de Lima KA, Dykstra T, Wall M, et al. Functional characterization of the dural sinuses as a neuroimmune interface. Cell. 2021;184(4):1000-16 e27. Epub 2021/01/29. doi: 10.1016/j.cell.2020.12.040. PubMed PMID: 33508229; PubMed Central PMCID: PMCPMC8487654.

6. Drieu A, Du S, Storck SE, Rustenhoven J, Papadopoulos Z, Dykstra T, et al. Parenchymal border macrophages regulate the flow dynamics of the cerebrospinal fluid. Nature. 2022;611(7936):585-93. Epub 20221109. doi: 10.1038/s41586-022-05397-3. PubMed PMID: 36352225; PubMed Central PMCID: PMCPMC9899827.

7. Masuda T, Amann L, Monaco G, Sankowski R, Staszewski O, Krueger M, et al. Specification of CNS macrophage subsets occurs postnatally in defined niches. Nature. 2022;604(7907):740-8. Epub 20220420. doi: 10.1038/s41586-022-04596-2. PubMed PMID: 35444273.

8. Amann L, Fell A, Monaco G, Sankowski R, Wu HZQ, Jordao MJC, et al. Extrasinusoidal macrophages are a distinct subset of immunologically active dural macrophages. Sci Immunol. 2024;9(102):eadh1129. Epub 20241220. doi: 10.1126/sciimmunol.adh1129. PubMed PMID: 39705337.

9. Mrdjen D, Pavlovic A, Hartmann FJ, Schreiner B, Utz SG, Leung BP, et al. High-Dimensional Single-Cell Mapping of Central Nervous System Immune Cells Reveals

622 Distinct Myeloid Subsets in Health, Aging, and Disease. Immunity. 2018;48(2):380-95 e6.
623 Epub 20180206. doi: 10.1016/j.immuni.2018.01.011. PubMed PMID: 29426702.
624
625 10. Van Hove H, Martens L, Scheyltjens I, De Vlaminck K, Pombo Antunes AR, De
626 Prijck S, et al. A single-cell atlas of mouse brain macrophages reveals unique
627 transcriptional identities shaped by ontogeny and tissue environment. Nat Neurosci.
628 2019;22(6):1021-35. Epub 2019/05/08. doi: 10.1038/s41593-019-0393-4. PubMed PMID:
629 31061494.
630
631 11. Smyth LCD, Xu D, Okar SV, Dykstra T, Rustenhoven J, Papadopoulos Z, et al.
632 Identification of direct connections between the dura and the brain. Nature.
633 2024;627(8002):165-73. Epub 20240207. doi: 10.1038/s41586-023-06993-7. PubMed
634 PMID: 38326613.
635
636 12. Vara-Perez M, Movahedi K. Border-associated macrophages as gatekeepers of
637 brain homeostasis and immunity. Immunity. 2025;58(5):1085-100. Epub 20250504. doi:
638 10.1016/j.immuni.2025.04.005. PubMed PMID: 40324381; PubMed Central PMCID:
639 PMCPMC12094687.
640
641 13. Rua R, Lee JY, Silva AB, Swafford IS, Maric D, Johnson KR, et al. Infection drives
642 meningeal engraftment by inflammatory monocytes that impairs CNS immunity. Nat
643 Immunol. 2019;20(4):407-19. Epub 20190318. doi: 10.1038/s41590-019-0344-y.
644 PubMed PMID: 30886419; PubMed Central PMCID: PMCPMC6481670.
645
646 14. Rebejac J, Eme-Scolan E, Arnaud Paroutaud L, Kharbouche S, Teleman M,
647 Spinelli L, et al. Meningeal macrophages protect against viral neuroinfection. Immunity.
648 2022;55(11):2103-17 e10. Epub 20221101. doi: 10.1016/j.immuni.2022.10.005. PubMed
649 PMID: 36323311.
650
651 15. De Vlaminck K, Van Hove H, Kancheva D, Scheyltjens I, Pombo Antunes AR,
652 Bastos J, et al. Differential plasticity and fate of brain-resident and recruited macrophages
653 during the onset and resolution of neuroinflammation. Immunity. 2022;55(11):2085-102
654 e9. Epub 20221012. doi: 10.1016/j.immuni.2022.09.005. PubMed PMID: 36228615.
655
656 16. Pinho-Ribeiro FA, Deng L, Neel DV, Erdogan O, Basu H, Yang D, et al. Bacteria
657 hijack a meningeal neuroimmune axis to facilitate brain invasion. Nature.
658 2023;615(7952):472-81. Epub 20230301. doi: 10.1038/s41586-023-05753-x. PubMed
659 PMID: 36859544; PubMed Central PMCID: PMCPMC10593113.
660
661 17. Desai BN, Leitinger N. Purinergic and calcium signaling in macrophage function
662 and plasticity. Front Immunol. 2014;5:580. Epub 20141127. doi:
663 10.3389/fimmu.2014.00580. PubMed PMID: 25505897; PubMed Central PMCID:
664 PMCPMC4245916.
665
666 18. Zumerle S, Cali B, Munari F, Angioni R, Di Virgilio F, Molon B, et al. Intercellular
667 Calcium Signaling Induced by ATP Potentiates Macrophage Phagocytosis. Cell Rep.

2019;27(1):1-10 e4. doi: 10.1016/j.celrep.2019.03.011. PubMed PMID: 30943393; PubMed Central PMCID: PMCPMC6449513.

19. Seegren PV, Downs TK, Stremska ME, Harper LR, Cao R, Olson RJ, et al. Mitochondrial Ca(2+) Signaling Is an Electrometabolic Switch to Fuel Phagosome Killing. Cell Rep. 2020;33(8):108411. doi: 10.1016/j.celrep.2020.108411. PubMed PMID: 33238121; PubMed Central PMCID: PMCPMC7793167.

20. Nascimento Da Conceicao V, Sun Y, Ramachandran K, Chauhan A, Raveendran A, Venkatesan M, et al. Resolving macrophage polarization through distinct Ca(2+) entry channel that maintains intracellular signaling and mitochondrial bioenergetics. iScience. 2021;24(11):103339. Epub 20211023. doi: 10.1016/j.isci.2021.103339. PubMed PMID: 34816101; PubMed Central PMCID: PMCPMC8591423.

21. Taghdiri N, Calcagno DM, Fu Z, Huang K, Kohler RH, Weissleder R, et al. Macrophage calcium reporter mice reveal immune cell communication in vitro and in vivo. Cell Rep Methods. 2021;1(8). Epub 20211213. doi: 10.1016/j.crmeth.2021.100132. PubMed PMID: 35079727; PubMed Central PMCID: PMCPMC8786215.

22. Mehari FT, Miller M, Pick R, Bader A, Pekayvaz K, Napoli M, et al. Intravital calcium imaging in myeloid leukocytes identifies calcium frequency spectra as indicators of functional states. Sci Signal. 2022;15(744):eabe6909. Epub 20220726. doi: 10.1126/scisignal.abe6909. PubMed PMID: 35881691.

23. Seegren PV, Harper LR, Downs TK, Zhao XY, Viswanathan SB, Stremska ME, et al. Reduced mitochondrial calcium uptake in macrophages is a major driver of inflammaging. Nat Aging. 2023;3(7):796-812. Epub 20230605. doi: 10.1038/s43587-023-00436-8. PubMed PMID: 37277641; PubMed Central PMCID: PMCPMC10353943.

24. Vaeth M, Zee I, Concepcion AR, Maus M, Shaw P, Portal-Celhay C, et al. Ca2+ Signaling but Not Store-Operated Ca2+ Entry Is Required for the Function of Macrophages and Dendritic Cells. J Immunol. 2015;195(3):1202-17. Epub 20150624. doi: 10.4049/jimmunol.1403013. PubMed PMID: 26109647; PubMed Central PMCID: PMCPMC4506881.

25. Schappe MS, Stremska ME, Busey GW, Downs TK, Seegren PV, Mendu SK, et al. Efferocytosis requires periphagosomal Ca(2+)-signaling and TRPM7-mediated electrical activity. Nat Commun. 2022;13(1):3230. Epub 20220609. doi: 10.1038/s41467-022-30959-4. PubMed PMID: 35680919; PubMed Central PMCID: PMCPMC9184625.

26. Kaya Z, Belder N, Sever-Bahcekapili M, Erdener SE, Donmez-Demir B, Bagci C, et al. Spreading depolarization triggers pro- and anti-inflammatory signalling: a potential link to headache. Brain. 2025;148(7):2522-36. doi: 10.1093/brain/awaf015. PubMed PMID: 39823578; PubMed Central PMCID: PMCPMC12378585.

27. Harriott AM, Ayata C. Spreading depolarization as a therapeutic target in migraine. Nat Rev Neurol. 2025;21(10):529-43. Epub 20250814. doi: 10.1038/s41582-025-01128-0. PubMed PMID: 40813918.

28. Ren X, Manzanares LD, Piccolo EB, Urbanczyk JM, Sullivan DP, Yalom LK, et al. Macrophage-endothelial cell crosstalk orchestrates neutrophil recruitment in inflamed mucosa. J Clin Invest. 2023;133(15). Epub 20230801. doi: 10.1172/JCI170733. PubMed PMID: 37261911; PubMed Central PMCID: PMCPMC10378177.

29. Ishikawa-Ankerhold H, Busch B, Bader A, Maier-Begandt D, Dionisio F, Namineni S, et al. Novel multiphoton intravital imaging enables real-time study of Helicobacter pylori interaction with neutrophils and macrophages in the mouse stomach. PLoS Pathog. 2024;20(9):e1012580. Epub 20240930. doi: 10.1371/journal.ppat.1012580. PubMed PMID: 39348445; PubMed Central PMCID: PMCPMC11478878.

30. Chinnery HR, Ruitenberg MJ, McMenamin PG. Novel characterization of monocyte-derived cell populations in the meninges and choroid plexus and their rates of replenishment in bone marrow chimeric mice. J Neuropathol Exp Neurol. 2010;69(9):896-909. doi: 10.1097/NEN.0b013e3181edbc1a. PubMed PMID: 20720507.

31. Jung S, Aliberti J, Graemmel P, Sunshine MJ, Kreutzberg GW, Sher A, et al. Analysis of fractalkine receptor CX(3)CR1 function by targeted deletion and green fluorescent protein reporter gene insertion. Mol Cell Biol. 2000;20(11):4106-14. doi: 10.1128/MCB.20.11.4106-4114.2000. PubMed PMID: 10805752; PubMed Central PMCID: PMCPMC85780.

32. Roth TL, Nayak D, Atanasijevic T, Koretsky AP, Latour LL, McGavern DB. Transcranial amelioration of inflammation and cell death after brain injury. Nature. 2014;505(7482):223-8. Epub 2013/12/10. doi: 10.1038/nature12808. PubMed PMID: 24317693; PubMed Central PMCID: PMCPMC3930079.

33. Liu YU, Ying Y, Li Y, Eyo UB, Chen T, Zheng J, et al. Neuronal network activity controls microglial process surveillance in awake mice via norepinephrine signaling. Nat Neurosci. 2019;22(11):1771-81. Epub 20191021. doi: 10.1038/s41593-019-0511-3. PubMed PMID: 31636449; PubMed Central PMCID: PMCPMC6858573.

34. McKinsey GL, Lizama CO, Keown-Lang AE, Niu A, Santander N, Larpthaveesarp A, et al. A new genetic strategy for targeting microglia in development and disease. Elife. 2020;9. Epub 20200623. doi: 10.7554/eLife.54590. PubMed PMID: 32573436; PubMed Central PMCID: PMCPMC7375817.

35. Daigle TL, Madisen L, Hage TA, Valley MT, Knoblich U, Larsen RS, et al. A Suite of Transgenic Driver and Reporter Mouse Lines with Enhanced Brain-Cell-Type Targeting and Functionality. Cell. 2018;174(2):465-80 e22. doi: 10.1016/j.cell.2018.06.035. PubMed PMID: 30007418; PubMed Central PMCID: PMCPMC6086366.

36. Tiedt R, Schomber T, Hao-Shen H, Skoda RC. Pf4-Cre transgenic mice allow the generation of lineage-restricted gene knockouts for studying megakaryocyte and platelet function in vivo. Blood. 2007;109(4):1503-6. Epub 20061010. doi: 10.1182/blood-2006-04-020362. PubMed PMID: 17032923.

37. Umpierre AD, Bystrom LL, Ying Y, Liu YU, Worrell G, Wu LJ. Microglial calcium signaling is attuned to neuronal activity in awake mice. Elife. 2020;9. Epub 20200727. doi: 10.7554/eLife.56502. PubMed PMID: 32716294; PubMed Central PMCID: PMCPMC7402678.

38. Thrane AS, Rangroo Thrane V, Zeppenfeld D, Lou N, Xu Q, Nagelhus EA, et al. General anesthesia selectively disrupts astrocyte calcium signaling in the awake mouse cortex. Proc Natl Acad Sci U S A. 2012;109(46):18974-9. Epub 2012/11/01. doi: 10.1073/pnas.1209448109. PubMed PMID: 23112168; PubMed Central PMCID: PMCPMC3503159.

39. Zhou H, Neudecker V, Perez-Zoghbi JF, Brambrink AM, Yang G. Age-dependent cerebral vasodilation induced by volatile anesthetics is mediated by NG2(+) vascular mural cells. Commun Biol. 2024;7(1):1519. Epub 20241115. doi: 10.1038/s42003-024-07200-7. PubMed PMID: 39548262; PubMed Central PMCID: PMCPMC11568297.

40. Goldey GJ, Roumis DK, Glickfeld LL, Kerlin AM, Reid RC, Bonin V, et al. Removable cranial windows for long-term imaging in awake mice. Nature protocols. 2014;9(11):2515-38. Epub 2014/10/03. doi: 10.1038/nprot.2014.165. PubMed PMID: 25275789; PubMed Central PMCID: PMCPMC4442707.

41. Blaeser AS, Sugden AU, Zhao J, Carneiro-Nascimento S, Shipley FB, Carrie H, et al. Trigeminal afferents sense locomotion-related meningeal deformations. Cell Rep. 2022;41(7):111648. doi: 10.1016/j.celrep.2022.111648. PubMed PMID: 36384109.

42. Mi X, Chen AB, Duarte D, Carey E, Taylor CR, Braaker PN, et al. Fast, accurate, and versatile data analysis platform for the quantification of molecular spatiotemporal signals. Cell. 2025;188(10):2794-809 e21. Epub 20250408. doi: 10.1016/j.cell.2025.03.012. PubMed PMID: 40203826.

43. Leon Guerrero PA, Rasmussen JP, Peterman E. Calcium dynamics of skin-resident macrophages during homeostasis and tissue injury. Mol Biol Cell. 2024;35(12):br26. Epub 20241113. doi: 10.1091/mbc.E24-09-0420. PubMed PMID: 39535893; PubMed Central PMCID: PMCPMC11656469.

44. Paterson N, Lammermann T. Macrophage network dynamics depend on haptokinesis for optimal local surveillance. Elife. 2022;11. Epub 20220328. doi: 10.7554/eLife.75354. PubMed PMID: 35343899; PubMed Central PMCID: PMCPMC8963880.

45. Behmoaras J, Mulder K, Ginhoux F, Petretto E. The spatial and temporal activation of macrophages during fibrosis. Nature reviews. 2025. Epub 20250604. doi: 10.1038/s41577-025-01186-x. PubMed PMID: 40467841.

46. Gao YR, Drew PJ. Effects of Voluntary Locomotion and Calcitonin Gene-Related Peptide on the Dynamics of Single Dural Vessels in Awake Mice. J Neurosci. 2016;36(8):2503-16. Epub 2016/02/26. doi: 10.1523/JNEUROSCI.3665-15.2016. PubMed PMID: 26911696; PubMed Central PMCID: PMCPMC4764666.

47. Levy D, Moskowitz MA. Meningeal Mechanisms and the Migraine Connection. Annual review of neuroscience. 2023. Epub 20230313. doi: 10.1146/annurev-neuro-080422-105509. PubMed PMID: 36913712.

48. Kursun O, Yemisci M, van den Maagdenberg A, Karatas H. Migraine and neuroinflammation: the inflammasome perspective. J Headache Pain. 2021;22(1):55. Epub 20210610. doi: 10.1186/s10194-021-01271-1. PubMed PMID: 34112082; PubMed Central PMCID: PMCPMC8192049.

49. Schain AJ, Melo-Carrillo A, Borsook D, Grutzendler J, Strassman AM, Burstein R. Activation of pial and dural macrophages and dendritic cells by cortical spreading depression. Ann Neurol. 2018;83(3):508-21. Epub 2018/02/03. doi: 10.1002/ana.25169. PubMed PMID: 29394508; PubMed Central PMCID: PMCPMC5965700.

50. Kipnis J. The anatomy of brainwashing. Science. 2024;385(6707):368-70. Epub 20240725. doi: 10.1126/science.adp1705. PubMed PMID: 39052816.

51. Chauhan A, Sun Y, Sukumaran P, Quenum Zangbede FO, Jondle CN, Sharma A, et al. M1 Macrophage Polarization Is Dependent on TRPC1-Mediated Calcium Entry. iScience. 2018;8:85-102. Epub 20180920. doi: 10.1016/j.isci.2018.09.014. PubMed PMID: 30293012; PubMed Central PMCID: PMCPMC6174824.

52. Zhao J, Levy D. Cortical Spreading Depression Promotes Persistent Mechanical Sensitization of Intracranial Meningeal Afferents: Implications for the Intracranial Mechanosensitivity of Migraine. eNeuro. 2016;3(6):ENEURO.0287-16.2016. Epub 2017/01/28. doi: 10.1523/ENEURO.0287-16.2016. PubMed PMID: 28127585; PubMed Central PMCID: PMCPMC5242377.

53. Blaeser AS, Zhao J, Sugden AU, Carneiro-Nascimento S, Andermann ML, Levy D. Sensitization of meningeal afferents to locomotion-related meningeal deformations in a migraine model. Elife. 2024;12. Epub 20240208. doi: 10.7554/eLife.91871. PubMed PMID: 38329894; PubMed Central PMCID: PMCPMC10942541.

54. Zhao J, Levy D. The CGRP receptor antagonist BIBN4096 inhibits prolonged meningeal afferent activation evoked by brief local K(+) stimulation but not cortical spreading depression-induced afferent sensitization. Pain Rep. 2018;3(1):e632. Epub

2018/02/13. doi: 10.1097/PR9.0000000000000632. PubMed PMID: 29430561; PubMed Central PMCID: PMCPMC5802320.

55. Deng L, Gillis JE, Chiu IM, Kaplan DH. Sensory neurons: An integrated component of innate immunity. Immunity. 2024;57(4):815-31. doi: 10.1016/j.immuni.2024.03.008. PubMed PMID: 38599172.

56. Jin X, Morais A, Sasaki Y, Zhai Q, Banerjee P, Harriott A, et al. Small-molecule CGRP antagonist atogepant does not affect cortical spreading depression susceptibility in rats. J Headache Pain. 2025;26(1):177. Epub 20250805. doi: 10.1186/s10194-025-02127-8. PubMed PMID: 40764901; PubMed Central PMCID: PMCPMC12326636.

57. Rustenhoven J, Kipnis J. Brain borders at the central stage of neuroimmunology. Nature. 2022;612(7940):417-29. Epub 20221214. doi: 10.1038/s41586-022-05474-7. PubMed PMID: 36517712; PubMed Central PMCID: PMCPMC10205171.

58. Min H, O'Neil SM, Xu L, Moseman EA, Kurtzberg J, Filiano AJ. Mural cells interact with macrophages in the dura mater to regulate CNS immune surveillance. J Exp Med. 2024;221(2). Epub 20240109. doi: 10.1084/jem.20230326. PubMed PMID: 38193859; PubMed Central PMCID: PMCPMC10783178.

59. Dalmau Gasull A, Glavan M, Samawar SKR, Kapupara K, Kelk J, Rubio M, et al. The niche matters: origin, function and fate of CNS-associated macrophages during health and disease. Acta Neuropathol. 2024;147(1):37. Epub 20240212. doi: 10.1007/s00401-023-02676-9. PubMed PMID: 38347231; PubMed Central PMCID: PMCPMC10861620.

60. Atcha H, Jairaman A, Holt JR, Meli VS, Nagalla RR, Veerasubramanian PK, et al. Mechanically activated ion channel Piezo1 modulates macrophage polarization and stiffness sensing. Nat Commun. 2021;12(1):3256. Epub 20210531. doi: 10.1038/s41467-021-23482-5. PubMed PMID: 34059671; PubMed Central PMCID: PMCPMC8167181.

61. Tong L, Hill RA, Damisah EC, Murray KN, Yuan P, Bordey A, et al. Imaging and optogenetic modulation of vascular mural cells in the live brain. Nature protocols. 2021;16(1):472-96. Epub 20201209. doi: 10.1038/s41596-020-00425-w. PubMed PMID: 33299155.

62. Semyanov A, Verkhratsky A. Astrocytic processes: from tripartite synapses to the active milieu. Trends Neurosci. 2021;44(10):781-92. Epub 20210831. doi: 10.1016/j.tins.2021.07.006. PubMed PMID: 34479758.

63. Takano T, Tian GF, Peng W, Lou N, Lovatt D, Hansen AJ, et al. Cortical spreading depression causes and coincides with tissue hypoxia. Nat Neurosci. 2007;10(6):754-62. Epub 2007/05/01. doi: 10.1038/nn1902. PubMed PMID: 17468748.

64. Rosic B, Dukefoss DB, Abjorsbraten KS, Tang W, Jensen V, Ottersen OP, et al. Aquaporin-4-independent volume dynamics of astroglial endfeet during cortical spreading depression. Glia. 2019;67(6):1113-21. Epub 2019/02/23. doi: 10.1002/glia.23604. PubMed PMID: 30791140; PubMed Central PMCID: PMCPMC6594042.

65. Lu YZ, Nayer B, Singh SK, Alshoubaki YK, Yuan E, Park AJ, et al. CGRP sensory neurons promote tissue healing via neutrophils and macrophages. Nature. 2024;628(8008):604-11. Epub 20240327. doi: 10.1038/s41586-024-07237-y. PubMed PMID: 38538784; PubMed Central PMCID: PMCPMC11023938.

66. Hasegawa T, Lee CYC, Hotchen AJ, Fleming A, Singh R, Suzuki K, et al. Macrophages and nociceptor neurons form a sentinel unit around fenestrated capillaries to defend the synovium from circulating immune challenge. Nat Immunol. 2024;25(12):2270-83. Epub 20241125. doi: 10.1038/s41590-024-02011-8. PubMed PMID: 39587345; PubMed Central PMCID: PMCPMC11588661.

67. Fattori V, Zaninelli TH, Rasquel-Oliveira FS, Heintz OK, Jain A, Sun L, et al. Nociceptor-to-macrophage communication through CGRP/RAMP1 signaling drives endometriosis-associated pain and lesion growth in mice. Sci Transl Med. 2024;16(772):eadk8230. Epub 20241106. doi: 10.1126/scitranslmed.adk8230. PubMed PMID: 39504351.

## Funding

The study was supported by NIH grants: R21NS130561; R01NS115972 and R01NS133625 to D.L.

## Authors information

D.L. conceived the project. S.C-N and D.L. wrote the manuscript. S.C-N performed two-photon imaging and data analysis with help from D.L. S.C-N, C.W., and A.G. performed surgeries.

**Authors and affiliations**

[1]Department of Anesthesia, Critical Care and Pain Medicine, Beth Israel Deaconess Medical Center, Harvard Medical School, Boston, United States

## Corresponding author

Correspondence to: dlevy1@bidmc.harvard.edu (Dan Levy)

## Competing interests

The authors declare that they have no competing interests.

**Supplementary video legends:**

**Video S1. Macrophage $Ca^{2+}$ dynamics in homeostatic meninges of awake mice**

Example two-photon imaging showing $Ca^{2+}$ activity in perivascular and non-perivascular meningeal macrophages.

**Video S2. Acute and persistent changes in meningeal macrophage $Ca^{2+}$ activity in response to CSD.**

Example two-photon imaging of meningeal macrophage $Ca^{2+}$ activity at baseline, during, and following CSD. The arrow indicates a macrophage showing an acute $Ca^{2+}$ elevation, the arrowhead depicts a delayed and persistent $Ca^{2+}$ elevation, and the asterisk, a macrophage showing a persistent decreased $Ca^{2+}$ activity.